


## Microstructure-Assisted Laser-Driven Photonuclear Pulsed Neutron Source

X.R. Jiang<sup>1</sup>, D.B. Zou<sup>1,\*</sup>, Z.J. Zhao<sup>1</sup>, L.X. Hu<sup>1</sup>, P. Han<sup>1</sup>, J.Q. Yu<sup>2</sup>, T.P. Yu<sup>1</sup>, Y. Yin<sup>1</sup> and F.Q. Shao<sup>1</sup>

<sup>1</sup>*Department of Physics, National University of Defense Technology, Changsha 410073, China*

<sup>2</sup>*School of Physics and Electronics, Hunan University, Changsha, 410082, China*

 (Received 14 October 2020; revised 1 February 2021; accepted 18 February 2021; published 11 March 2021)

A scheme for a high-yield photonuclear pulsed neutron source is proposed by use of a relativistic femtosecond laser interacting with a microstructure target combined with a high- $Z$  converter. By using three-dimensional particle-in-cell and Monte Carlo simulations, we find that bright  $\gamma$  rays are emitted by bremsstrahlung radiation when energetic dense electron bunches pulled out from the microstructure target pass through the converter. A large number of neutrons are thus induced via photonuclear reactions. With a laser of intensity of approximately  $3.4 \times 10^{21}$  W/cm<sup>2</sup> and energy of approximately 6.2 J, a neutron pulse of yield as high as  $1.9 \times 10^8$  J<sup>-1</sup> and duration of approximately 45 ps can be obtained. This scheme could be realized in laboratories with current multipetawatt laser facilities.

DOI: [10.1103/PhysRevApplied.15.034032](https://doi.org/10.1103/PhysRevApplied.15.034032)

### I. INTRODUCTION

The development of a tabletop particle accelerator [1,2] based on ultrahigh-power ultrashort laser pulse has opened a window for exploring alternative neutron-production techniques [3–9]. Compared with traditional neutron sources, laser-driven neutron sources have the advantages of small spot size, short duration, and high brightness [3,8]. These features are favored by many applications, such as fast-neutron resonance radiography [10], nuclear medicine [11], and neutron scattering [12]. There are two main laser-based methods of pulsed neutron production: beam-target fusion [3–5] and photonuclear reaction [6–9]. In general, the beam-target neutron source has higher neutron yield and energy as well as better direction [3]. However, the pulse duration of fusion neutrons is usually a few hundred picoseconds [8]. In contrast, it is easier to achieve a pulse duration as short as tens of picoseconds for photoneutrons [8], which is beneficial for high time resolution in neutron imaging. Furthermore, the photoneutron energy is typically determined by the gaps between the energy levels of the initial nucleus and the final nucleus [13]. The neutron spectrum usually exhibits a stable structure with energy ranging from kiloelectronvolts (keV) to megaelectronvolts (MeV), which is independent of the effective temperature of  $\gamma$  photons and depends only on the material properties [14]. The photonuclear pulsed neutron source is therefore suitable for some special applications, such as a neutron detector [15] and nuclear-cross-section measurement [16].

The number and temperature of hot electrons are of great importance for obtaining high-yield photonuclear neutrons. For a high- $Z$  converter material, the cross section of the photonuclear reaction usually peaks at a photon energy on the order of a dozen MeV [17]. This requires that a large number of hot electrons can be accelerated to a reasonably high temperature. Laser wakefield acceleration [18] is an effective way to accelerate the negatively charged electrons to energies of hundreds of MeV or even GeV. Unfortunately, the total electric charge in laser wakefield acceleration is very small due to the low initial plasma density. The attainable neutron yield per joule of laser energy  $N_n/\varepsilon_L$  is thus limited to approximately  $10^6$  J<sup>-1</sup> in experiments [9], where  $\varepsilon_L$  is the laser energy. The ultraintense laser interacting with a solid target allows efficient coupling of energy from the laser to relativistic hot electrons with a higher number density via  $J \times B$  heating [19] or other mechanisms [20]. A recent experiment demonstrated that  $N_n/\varepsilon_L$  can be as high as approximately  $10^7$  J<sup>-1</sup>, which is the experimental record for laser-driven photonuclear neutrons reported to date [8]. However, great increase of the achievable neutron yield remains a challenging endeavor since the laser beam is strongly reflected by the front surface of the target, especially for an ultrashort, ultraintense (USUI) laser pulse interacting with a flat target structure. Recently, microscale surface structures have attracted much interest to increase the energy-conversion efficiencies in acceleration of electrons [21,22], ions [23,24], and positrons [25] as well as the production of x-ray or  $\gamma$ -ray radiation [26,27]. For instance, three-dimensional printed microtube or micropillar targets with a length of more than 10  $\mu$ m and inner diameters of several microns have been applied in experiments to enhance

\*debinzou@nudt.edu.cn

charged-particle acceleration [21,28] and achieve extreme pressure conditions [29], respectively.

In this paper, we propose an efficient scheme for generating a high-yield photonuclear pulsed neutron source via the interaction of an ultraintense femtosecond laser pulse with a microstructure target (MST). The setup is illustrated in Fig. 1. The MST is a solid planar end plate with a fabricated micron-scale metal wire array. Simulation results show the forward hot electrons generated from the MST have higher energy, temperature and laser-to-electron energy conversion efficiency compared with those generated from a planar geometry. When these electrons shoot into the subsequent high- $Z$  converter, bright  $\gamma$  rays with high temperature are emitted by bremsstrahlung radiation. A large number of neutrons are then induced from the interaction of these photons with their surrounding heavy nuclei. For the optimal MST parameters, we find that  $N_n/\varepsilon_L$  is as high as approximately  $10^8 \text{ J}^{-1}$  and the pulse duration is approximately 45 ps.

## II. MODEL AND SIMULATION PARAMETERS

To explore the dynamics of the electrons generated in the MST, we first perform numerical simulations with the three-dimensional particle-in-cell (PIC) code EPOCH [30]. The simulation box size is  $x \times y \times z = 50\lambda_0 \times 12\lambda_0 \times 12\lambda_0$ , with 32 cells per  $\lambda_0$ , where  $\lambda_0 = 0.8 \mu\text{m}$  is the laser wavelength. Each cell has 35 macroparticles. The cylindrical Cu wires, of length  $L_0 = 10\lambda_0$ , radius  $r_0 = 0.2\lambda_0$ , and transverse interval between the central axes of the adjacent wires  $d_0 = 1.9\lambda_0$ , are located between  $x_0 = 5\lambda_0$  and  $x_1 = 15\lambda_0$ . A Cu end plate of thickness  $L_1 = 1.0\lambda_0$  is used to support the metal wires, and is attached directly to the wire array. The MST is assumed to be a preionized  $\text{Cu}^{5+}$  plasma with density  $n_e = 5n_i = 200n_c$ , where  $n_c = m_e\omega_0^2/4\pi e^2$  is the critical plasma density, where  $\omega_0$  is the laser frequency and  $e$  and  $m_e$  are the electron charge

and rest mass, respectively. A  $p$ -polarized laser pulse is focused on the front surface of the wires and is normally incident into the MST. The amplitude profile of the laser pulse is given by  $a = a_0 \sin^2(\pi t/2\tau_0) \exp[-(r/\sigma_0)^2]$ , where the normalized laser amplitude  $a_0 = eE_L/m_e\omega_0 c = 40$ , where  $E_L$  is the laser electric field and  $c$  is the speed of light in a vacuum. The focal spot radius  $\sigma_0 = 3\lambda_0$  and the pulse duration  $\tau_0 = 10T_0$ , where  $T_0 = 2.67 \text{ fs}$  is the laser period. This corresponds to a laser intensity of approximately  $3.4 \times 10^{21} \text{ W/cm}^2$ , power of approximately 0.31 PW, and total energy  $\varepsilon_L \approx 6.2 \text{ J}$ . For comparison, we also simulate the planar-target (PT) case with the same laser parameters. We emphasize that the collision process is not considered in our PIC simulations since the plasmas will be heated to a high temperature of several MeVs or more in a very short time for relativistic femtosecond-laser-plasma interaction. The collision cross section is therefore very low, so physical collisional heating is negligible [31].

We then use the Monte Carlo (MC) code FLUKA [32] to investigate the  $\gamma$ -photon and photoneutron generation. The converter is composed of the high- $Z$  metal Ta of thickness  $L_2 = 2 \text{ cm}$  and transverse size  $4 \times 4 \text{ cm}^2 = 16 \text{ cm}^2$ . Ta material is chosen due to its large photonuclear reaction cross section. In the MC simulation, the laser-accelerated electron beam can be regarded as a point source since its spatial size (on the micron scale) is much smaller than that of the converter. When the electron energy and angular distributions from the PIC simulation are input into the MC simulation, a large number of random samples (here  $5 \times 10^5$ ) are used to reproduce their distributions and calculate the averaged probability of neutron production. The distance  $\Delta L$  between the MST and the converter will affect the electron distribution and final photoneutron generation. In Fig. 1, the MST and high- $Z$  converter are separated only to show the whole physical process clearly. Actually, the electron source is initially located at the front surface of the converter (i.e.,  $\Delta L = 0$ ).

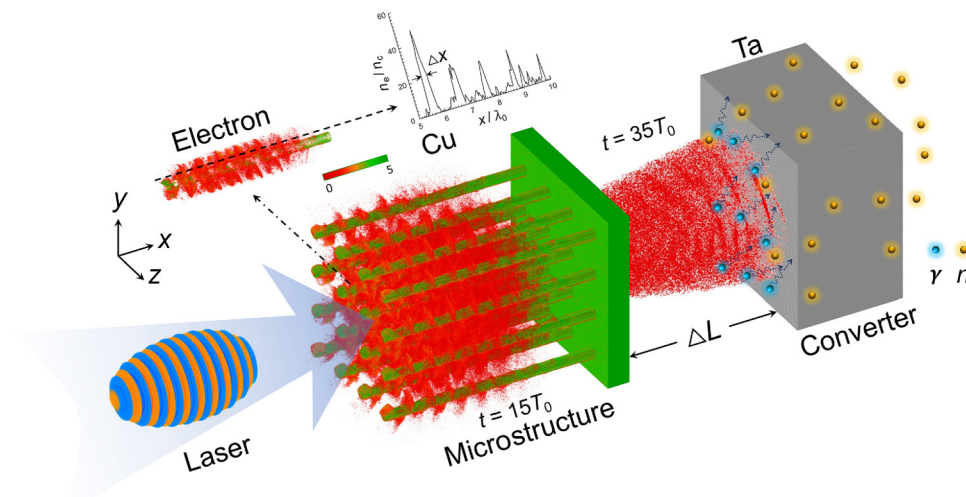


FIG. 1. The proposed scheme for high-yield photonuclear neutron generation. A relativistic femtosecond laser pulse irradiates a Cu wire-array MST combined with a high- $Z$  Ta converter normally (not to scale). The density profiles  $\ln(n_e/n_c)$  of the wire electrons at  $t = 15T_0$  (before  $x = 15\lambda_0$ ) and at  $t = 35T_0$  (after  $x = 16\lambda_0$ ) obtained from PIC simulation are also shown. The inset at the top gives the appearance of a particular wire within the laser focal spot and the axial profile of the electron bunch along the  $y = 0.4\lambda_0$  and  $z = -0.95\lambda_0$  direction.

The above laser-target parameters are used in Secs. III A and III B. In Sec. III C, to investigate the dependence of the electron temperature  $k_B T_e$  (where  $k_B$  is the Boltzmann constant), photon temperature  $k_B T_\gamma$ , and neutron yield  $N_n$  on the laser intensity, only  $a_0$  is changed, while all the other parameters remain unchanged. For the influence of the wire size and plasma density in Sec. III D, the laser amplitude is fixed at  $a_0 = 40$ . We then vary one of the parameters in turn, and other parameters are the same as in Secs. III A and III B.

### III. RESULTS AND DISCUSSION

#### A. Acceleration of dense electron bunches

For the MST, the distributions of the electron density at  $t = 15T_0$  and the transverse electric field  $E_y$  of the laser at  $t = 20T_0$  are shown in Fig. 1 and Figs. 2(a) and 2(b), respectively. One can see that many dense electron bunches are pulled out by the transverse electric field of the  $p$ -polarized laser pulse enfolding the metal wires. This phenomenon is consistent with previous results regarding a relativistic laser interacting with microtube or micropillar targets [23,33–37], and originates from the breaking of stimulated Langmuir oscillation for sufficiently large laser amplitudes [38]. For the highest-density peak, the width of the laminar electron layer  $\Delta x \approx 0.2 \mu\text{m}$  [full width at half maximum (FWHM)], corresponding to a duration  $\Delta t \approx \Delta x/c \approx 670$  as. Usually, attosecond dense electron

layers are generated from the left tip of the wires and are then accelerated forward [37]. The entire temporal width of the electron bunches  $\tau_e$  should thus be comparable to that of the laser pulse; that is,  $\tau_e \approx 2\tau_0 = 20T_0$ . The magnitude of transverse electric field remains almost unchanged, suggesting that the amplification effect of the laser amplitude from the nonlinear focusing of light in the hollow plasma channels is not significant. The channels between the adjacent wires can be regarded as rectangular plasma waveguides. Thus, the transverse magnetic (TM) mode of the waveguide will be excited as the laser pulse is passing through the channels [39]. We find that some of these pulled-out electrons can be trapped in the longitudinal electric field  $E_x^{\text{TM}}$  of TM modes, as shown in Figs. 2(d) and 2(e). They can be synergistically accelerated forward by this field as well as the laser ponderomotive force. Figures 2(c) and 2(f) show the phase-space distributions of the transverse electron momentum  $p_y$  and longitudinal electron momentum  $p_x$  at  $t = 25T_0$ . We see that  $p_x$  is much greater than  $p_y$ , indicating that the longitudinal electron acceleration is more dominant. The maximum longitudinal momentum  $p_{x,\text{max}}$  of hot electrons for the MST can be approximated by [23,35]

$$p_{x,\text{max}} = \begin{cases} a_0^2 m_e c / 2 + e \langle E_x^{\text{TM}} \rangle t_a & (a_0 < a_{\text{cr}}), \\ \left( a_0 / \sqrt{v_{\text{ph}}^2 / c^2 - 1} \right) m_e c + e \langle E_x^{\text{TM}} \rangle t_a & (a_0 \geq a_{\text{cr}}), \end{cases} \quad (1)$$

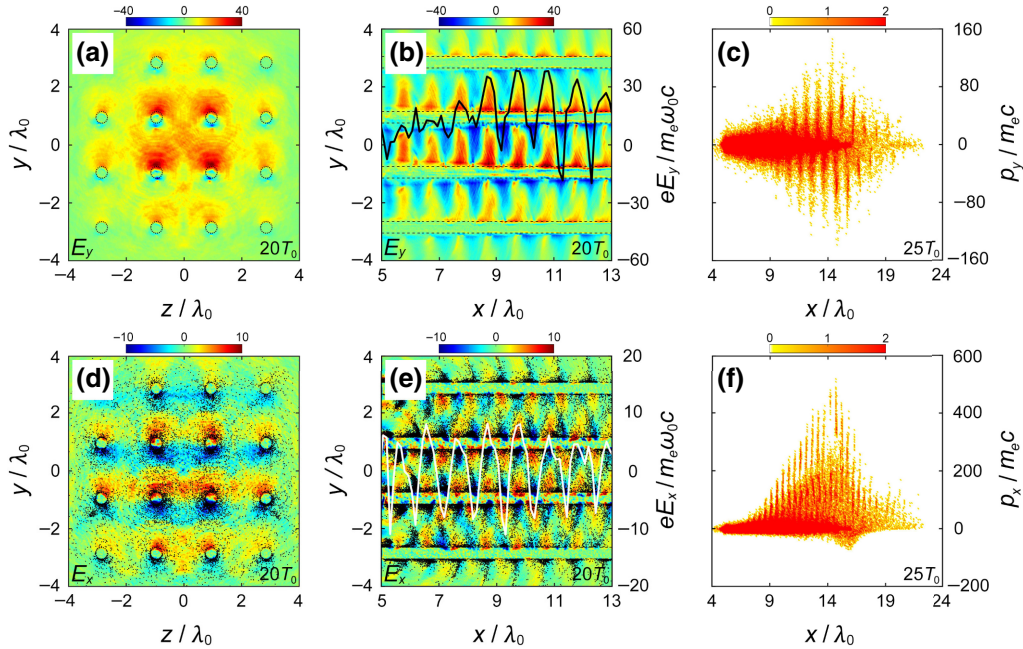


FIG. 2. Distributions of the (a),(b) transverse and (d),(e) longitudinal electric fields at  $t = 20T_0$  for the MST case along (a),(d) the cross section at  $x = 9.75\lambda_0$  and (b),(e) the longitudinal section at  $z = -0.95\lambda_0$ . The dashed black lines mark the outer edges of the Cu wires. The black and white curves in (b),(e) (corresponding to the right  $y$  axes) are the axial profiles along the  $y = -0.7\lambda_0$  and  $z = -0.95\lambda_0$  direction. The black dots in (d),(e) represent typical trapped electrons. The (c) transverse and (f) longitudinal momenta of the electrons pulled out from Cu wires by the laser at  $t = 25T_0$ . Here, all the electric fields and momenta are normalized by  $E_0 = m_e \omega_0 c / e$  and  $p_0 = m_e c$ , respectively.



where  $E_x^{\text{TM}} \approx E_L / [4(d_0 - 2r_0)^2 / \lambda_0^2 - 1]^{1/2}$ ,  $\langle E_x^{\text{TM}} \rangle \approx E_x^{\text{TM}} / 2$  is the averaged longitudinal electric field, and  $t_a = \min(L_0/c, t_d)$  and  $t_d = 2\lambda_0 / (v_{\text{ph}} - c)$  are the acceleration and dephasing times, respectively. Here,  $a_{\text{cr}} = [2c / (v_{\text{ph}} - c)]^{1/2}$  is the threshold amplitude above which the effect of the phase velocity,  $v_{\text{ph}} \approx [1 + \lambda_0^2 / 8(d_0 - 2r_0)^2] c$ , exceeding  $c$  should be taken into account. Taking  $a_0 = 40$ ,  $L_0 = 10\lambda_0$ ,  $d_0 = 1.9\lambda_0$ , and  $r_0 = 0.2\lambda_0$ , we obtain  $p_{x,\text{max}} = 560m_e c$ , which fits well with Fig. 2(f).

At  $t = 35T_0$ , most of the energetic electrons have penetrated through the attached end plate (shown in Fig. 1) and are therefore responsible for inducing the following  $\gamma$ -photon generation and photoneutron generation. Thus, we need to consider only the hot electrons behind the target ( $x > 16\lambda_0$ ) with longitudinal momenta  $p_x > 0$ . Their spectra  $dN_e/dE_e$  are shown in Fig. 3(a), which shows that the electron temperature  $k_B T_e$  and maximum energy  $E_{e,\text{max}}$  are as high as 22.5 and 200 MeV, respectively, in the MST case. They are much greater than in the PT case due to effective electron acceleration in the plasma waveguide. Figure 3(b) presents the efficiency of energy conversion  $\eta_e$  from the laser to electrons with energies higher than a certain threshold  $E_p$ . For different  $E_p$  values, we see that

all the  $\eta_e$  values for the MST case are much higher than the values for the PT case. In particular, about 10.5% of laser energy is delivered to electrons of energy higher than  $E_p = 25$  MeV with use of the microstructure. In contrast,  $\eta_e$  is close to 0 for the PT case. We also measure the efficiency of energy conversion from the laser to all the particles (i.e., total laser absorption rate  $\eta_t$ ) for both cases. It is found that  $\eta_t$  for the MST case is about 76%, which is 1 order of magnitude higher than 7% for the PT case. We emphasize that  $\eta_t$  for the PT case is much lower than that in Ref. [40]. This is because for an USUI laser pulse the electrons cannot receive all the energy from the ponderomotive potential of the laser [23].

## B. Generation of $\gamma$ photons and photonuclear neutrons

Figure 3(c) shows the spectra of photons from MC simulations for both cases. We can see that a large number of  $\gamma$  photons are emitted by bremsstrahlung radiation for the MST. The photon temperature  $k_B T_\gamma = 16$  MeV is far greater than the 1.3 MeV in the PT case. The highest efficiency of energy conversion from the laser to  $\gamma$  photons  $\eta_\gamma$  is about 2.5%. Synchrotron photons are also produced in the process of the laser interacting with the MST. However,

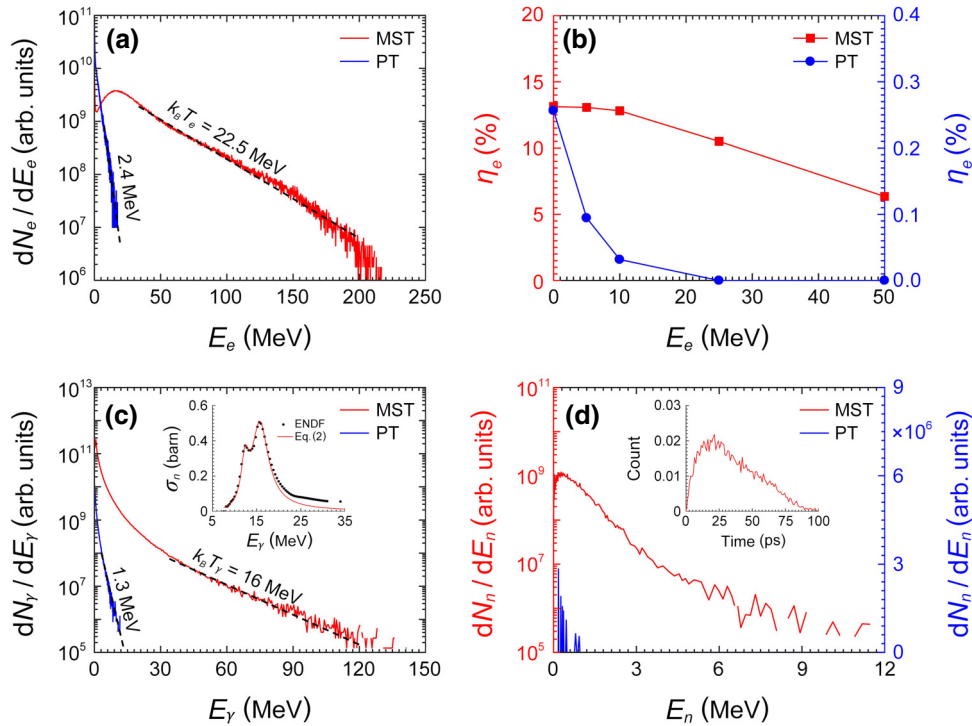


FIG. 3. Spectra of (a) electrons, (c) photons, and (d) neutrons as well as (b) the laser-to-electron energy-conversion efficiency  $\eta_e$  for electrons with energy higher than a certain threshold  $E_p = 0, 5, 10, 25,$  and  $50$  MeV for the MST case (red line) and the PT case (blue line). The blue curves in (b),(d) refer to the right  $\gamma$  axes. The inset in (c) shows the photonuclear cross section in Ta material, and the black dots and the red line correspond to Evaluated Nuclear Data File data [41] and Eq. (2), respectively. The inset in (d) gives the temporal evolution of the normalized neutron number. Here, the electrons in (a),(b) are behind the target ( $x > 16\lambda_0$ ) and have positive longitudinal momenta ( $p_x > 0$ ). The black lines around the curves in (a),(c) label the electron and photon temperatures, and the time chosen corresponds to their highest values.

these photons are concentrated mainly in the x-ray waveband (i.e., the photon energy  $E_\gamma < 1$  MeV) when the laser intensity is less than  $10^{22}$  W/cm<sup>2</sup> (i.e.,  $a_0 < 70$ ) [26]. Their influence for photon neutron generation is therefore negligible since the threshold energy of photons for photonuclear reaction  $E_{\gamma,\text{th}}$  is greater than 7 MeV, as presented in the inset in Fig. 3(c). In the semiclassical theory of the interaction between photons and nuclei, the shape of the photonuclear cross section  $\sigma_n$  consists of the superposition of the Lorentz curves [17]:

$$\sigma_n(E_\gamma) = \sum_i \frac{\sigma_{n,\text{max},i}}{1 + (E_\gamma - E_{m,i})^2/E_\gamma^2 \Gamma_i^2} (E_\gamma > E_{\gamma,\text{th}}), \quad (2)$$

where  $E_{m,i}$  is the photon energy corresponding to the peak photonuclear cross section  $\sigma_{n,\text{max},i}$  and  $\Gamma_i$  is the FWHM of the Lorentz curve. These variables in Eq. (2) can be acquired by comparison with the Evaluated Nuclear Data File [41]. For Ta material, there are typically two peak photonuclear cross sections (i.e.,  $i = 2$ ). We then obtain  $E_{m,1} = 12.4$  MeV,  $\sigma_{n,\text{max},1} = 0.25$  b, and  $\Gamma_1 = 2.2$  MeV and  $E_{m,2} = 15.8$  MeV,  $\sigma_{n,\text{max},2} = 0.48$  b, and  $\Gamma_2 = 4.5$  MeV. Note that  $k_B T_\gamma = 16$  MeV for the MST is very close to the optimal photon energy  $E_m = 15.6$  MeV for the maximum  $\sigma_{n,\text{max}}$  in Ta material [also see the inset in Fig. 3(c)]. As a result, more neutrons are generated with a pulse duration of 45 ps FWHM, as shown in the inset in Fig. 3(d). For the MST, the neutron yield  $N_n$  is as high as  $1.2 \times 10^9$ , which is increased by about 4 orders of magnitude compared with the PT case. We note that  $N_n = 1.2 \times 10^9$  is only for the situation with  $\Delta L = 0$ . We also simulate the cases of different  $\Delta L$  and find that  $N_n$  is only slightly decreased when  $\Delta L$  is less than 0.1 cm ( $N_n \approx 1.15 \times 10^9$  at  $\Delta L = 0.1$  cm). However, it begins to decrease significantly as  $\Delta L$  becomes larger (e.g.,  $N_n \approx 1 \times 10^8$  at  $\Delta L = 10$  cm). Therefore, the optimal position for the converter is behind the Cu end plate (i.e.,  $\Delta L = 0$ ) to maximize the neutron yield.

For the MST, the accumulated fluences of electrons, photons, and neutrons projected on the  $x$ - $o$ - $y$  plane throughout the neutron-generation process are shown in Fig. 4. The fluence distributions of three species of particles show a candle-flame-like appearance. Most of the photons and neutrons are produced at the center of the flame. Their number density gradually decreases with increasing depth and radial distance from the  $y = 0$  axis.

### C. Scaling laws for the electron and photon temperatures, and neutron yield

We now examine the dependence of  $k_B T_e$  and  $k_B T_\gamma$  on  $a_0$  since  $N_n$  is closely related to the properties of hot electrons and photons. Figure 5(a) shows that  $k_B T_e$  scales as  $a_0$  for both cases. Even for an USUI laser pulse,  $k_B T_e$  (approximately equal to  $0.56a_0$  MeV) in the MST case is still

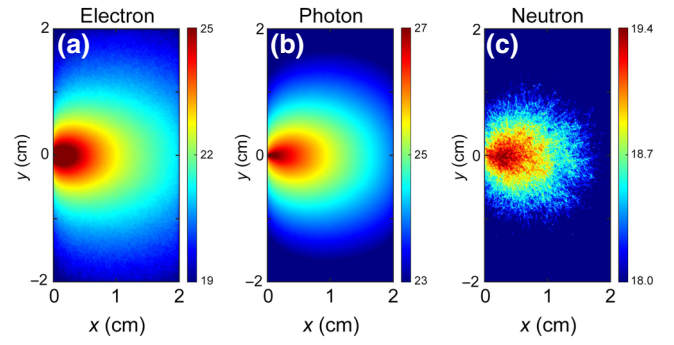


FIG. 4. The accumulated fluences (logarithmic scale) of (a) electrons, (b) photons, and (c) neutrons projected on the  $x$ - $o$ - $y$  plane from MC simulation for the MST.

greater than Wilks's ponderomotive scaling  $k_B T_e/m_e c^2 = (1 + a_0^2)^{1/2} - 1$  [42] and Kluge's scaling  $k_B T_e/m_e c^2 = 2\pi / \int_0^{2\pi} (1 + a_0^2 \sin^2 \omega_0 t)^{-1/2} dt - 1$  [43]. It is increased by almost 1 order of magnitude compared with  $k_B T_e \approx 0.06a_0$  MeV in the PT case. Note that  $k_B T_e \approx 0.06a_0$  MeV for the PT case agrees well with Beg's experimental fitting result  $k_B T_e/m_e c^2 = 0.47a_0^{2/3}$  [44] and Haines's relativistic model  $k_B T_e/m_e c^2 = (1 + 2^{1/2}a_0)^{1/2} - 1$  [45] due to inefficient laser-to-target energy coupling for an USUI laser pulse [23,35,45]. For the  $\gamma$  photons,  $k_B T_\gamma$  also varies linearly with increasing  $a_0$  for both cases and is slightly lower than  $k_B T_e$  due to the energy loss in the inelastic collision of particles. Benefiting from a significant increase of  $k_B T_e$ , we find that  $k_B T_\gamma \approx 0.38a_0$  MeV for the MST case is much greater than  $k_B T_\gamma \approx 0.02a_0$  MeV for the PT case. Differently from the linear relationship in Fig. 5(a), we see that  $N_n$  grows exponentially with  $a_0$ . However,  $N_n/\varepsilon_L$  gradually becomes saturated at approximately  $10^8$  J<sup>-1</sup> or even declines slightly when  $a_0 \geq 50$ . This is because there is an optimal photonuclear reaction cross section for Ta material. For  $a_0 \approx 50$ ,  $k_B T_e$  and  $k_B T_\gamma$  are closer to their optimal values for neutron generation.

The accurate evaluation for  $N_n$  depends on the entire electron-photon cascade and photon-matter interaction. In the following, we establish a simple theoretical model to estimate  $N_n$  in a convenient way. We assume that the electrons directly release relatively few neutrons and most of the neutrons are produced in the interaction between photons and nuclei [6]. The approximate expression for the integrated-over-angle bremsstrahlung cross section is [46]

$$\frac{d\sigma_\gamma}{dE_\gamma} = \alpha Z^2 \left( \frac{1}{E_\gamma} - \frac{\beta}{E_e} \right), \quad (3)$$

where  $\alpha \approx 0.011$  b and  $\beta \approx 0.83$  is a fitting constant based on the results of Seltzer and Berger [47]. By integrating Eq. (3) over  $dN_e/dE_e$ , we can obtain the spectral

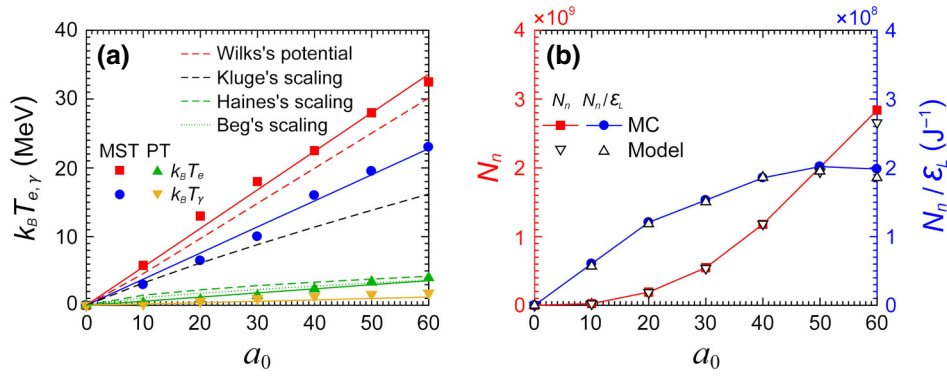


FIG. 5. (a) The highest electron (MST, red squares; PT, green triangles) and photon (MST, blue circles; PT, yellow triangles) temperatures for both cases versus laser amplitude  $a_0$ . The solid lines are the fitting results. For comparison, several existing scaling laws for  $k_B T_e$  for the laser-PT interaction are given, including Wilks's scaling (dashed red line) [42], Kluge's scaling (dashed black line) [43], Beg's empirical formula (dotted green line) [44], and Haines's model (dashed green line) [45]. (b) The neutron yield  $N_n$  (red squares) and the neutron yield per unit of laser energy  $N_n/\varepsilon_L$  (blue circles, corresponding to the right y axis) for the MST versus laser amplitude  $a_0$  from MC simulations. The hollow black triangles represent the estimated results from the analytical model.

distribution of photons as

$$\frac{dN_\gamma}{dE_\gamma} = n_a l \int_{E_\gamma}^{E_{e,\max}} \frac{d\sigma_\gamma}{dE_\gamma} \frac{dN_e}{dE_e} dE_e, \quad (4)$$

where  $n_a$  and  $l$  are the atomic density and thickness of the converter, and  $E_{e,\max}$  and  $dN_e/dE_e$  are obtained from PIC simulation. After integrating Eq. (2) over  $dN_\gamma/dE_\gamma$ , we obtain

$$N_n = \zeta n_a l \int_{E_{\gamma,\text{th}}}^{E_{\gamma,\max}} \sigma_n \frac{dN_\gamma}{dE_\gamma} dE_\gamma, \quad (5)$$

where  $E_{\gamma,\max}$  is the maximum photon energy.  $\zeta$  (here approximately 0.72 for Ta material) is a correction coefficient that takes into account other effects, such as photoelectric absorption [48] and positron generation [25], competing with neutron generation, and is usually less than 1. The above estimation is valid only for a thin converter with thickness far below the average range of electrons in the material and thus the energy loss in the stopping process is ignored. In general, the Ta target is a few centimeters thick to maximize  $N_n$ , and thus the energy loss of hot electrons should be taken into account. For large thickness, the converter can be divided into  $s$  equal layers,

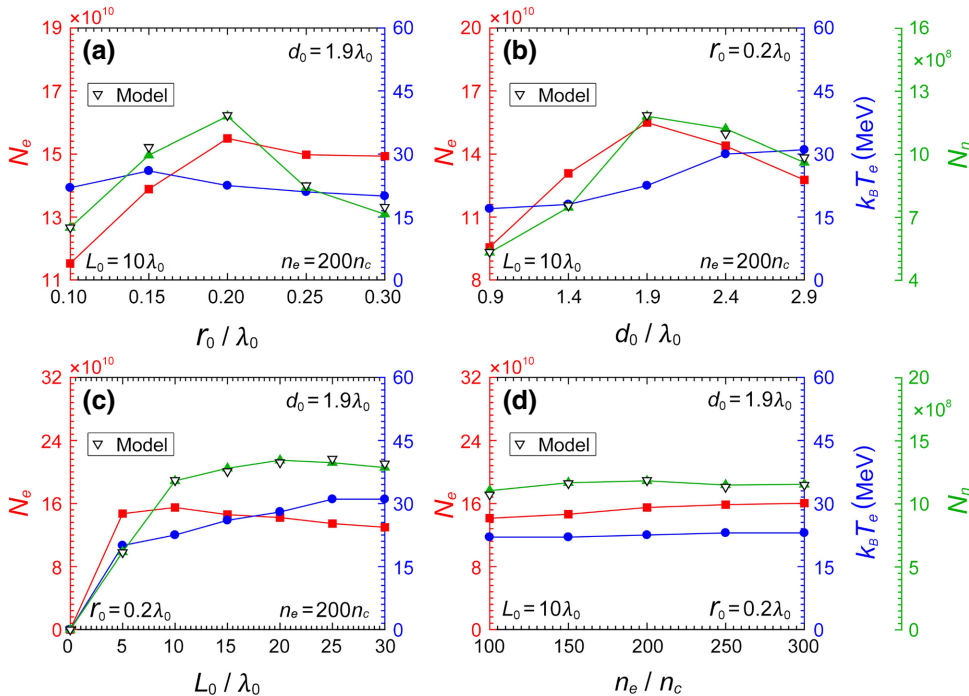


FIG. 6. The number  $N_e$  (red squares) and temperature  $k_B T_e$  (blue circles) of the electrons, and neutron yield  $N_n$  (green triangles) for the MST as a function of (a) the radius  $r_0$ , (b) the transverse interval  $d_0$ , (c) the length  $L_0$ , and (d) the initial electron density  $n_e$  of the Cu wires. The electrons counted in the simulations are behind the target and have positive longitudinal momenta. The solid and hollow symbols correspond to simulations and the analytical model, respectively.

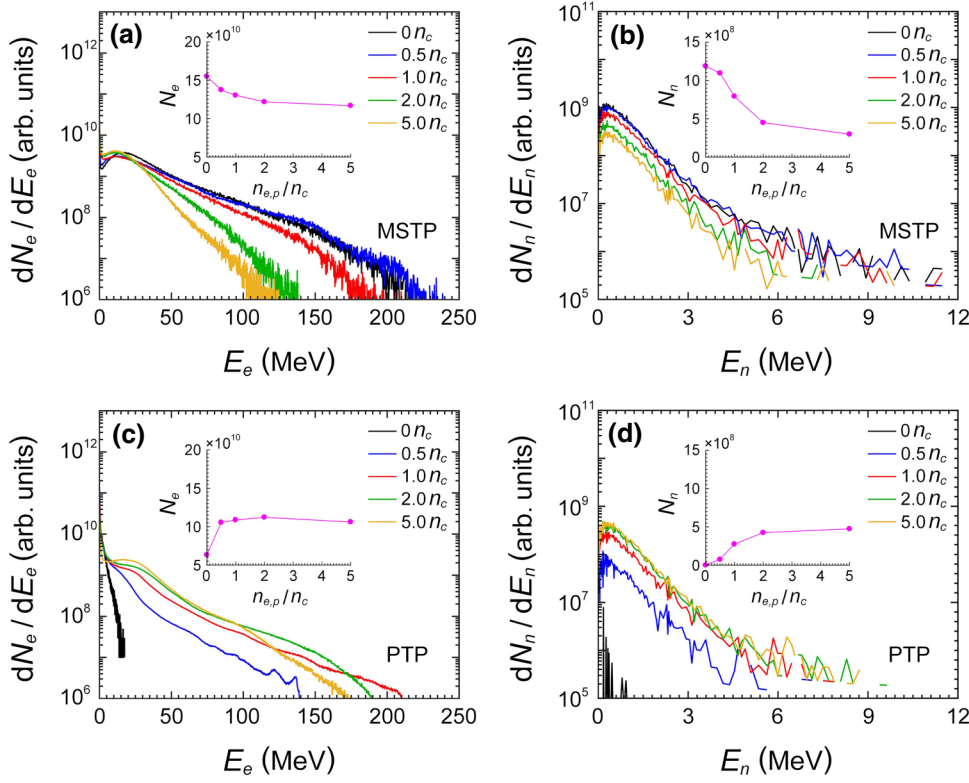


FIG. 7. Spectra of (a),(c) electrons that are behind the target and have positive longitudinal momenta and (b),(d) neutrons at different preplasma densities  $n_{e,p}$  for the MSTP and PTP cases. The moment chosen in (a),(c) corresponds to that for the highest electron temperature. The insets in (a)–(d) (pink circles and curves) show the dependence of the electron number and neutron yield as a function of the normalized preplasma density  $n_{e,p}/n_c$ .

and the thickness of each thin layer  $\Delta l = l/s$ . The electron spectrum in the  $i$ th layer  $dN_{e,i}/dE_{e,i}$  is then obtained with the initial  $dN_e/dE_e$  and the stopping power  $dE_e/dx$  of electrons in the converter material [49]. Thus, the photon spectrum of bremsstrahlung radiation  $dN_{\gamma,i}/dE_{\gamma,i}$  in the  $i$ th layer can be given by use of  $\Delta l$  to replace  $l$  in Eq. (4), giving

$$\frac{dN_{\gamma,i}}{dE_{\gamma,i}} = n_a \Delta l \int_{E_{\gamma,i}}^{E_{e,i,\max}} \frac{d\sigma_{\gamma}}{dE_{\gamma,i}} \frac{dN_{e,i}}{dE_{e,i}} dE_{e,i}. \quad (6)$$

The total neutron yield can therefore be rewritten as

$$N_n = \sum_i N_{n,i} = \sum_i \xi n_a (l - i\Delta l) \int_{E_{\gamma,\text{th}}}^{E_{\gamma,i,\max}} \sigma_n \frac{dN_{\gamma,i}}{dE_{\gamma,i}} dE_{\gamma,i}, \quad (7)$$

where  $N_{n,i}$  and  $l - i\Delta l$  are the corresponding neutron yield and the path length of the photons in the  $i$ th layer, respectively. For a Ta converter,  $Z = 73$  and  $n_a \approx 5.5 \times 10^{22} \text{ cm}^{-3}$ , we can obtain the final  $N_n$  and  $N_n/\varepsilon_L$  according to Eq. (7). The hollow symbols in Fig. 5(b) show the analytical results, which are in good accordance with the results of the MC simulations.

#### D. Parametric effect

The parameters of the microplasma wires play a crucial role in the electron acceleration and subsequent neutron

generation. Figure 6 shows the influence of  $r_0$ ,  $d_0$ ,  $L_0$ , and  $n_e$  on  $N_e$ ,  $k_B T_e$ , and  $N_n$ . One can see that to provide more electrons and reduce light reflection, the optimal radius  $r_0 \approx 0.2\lambda_0$  for the highest  $N_e$  is only a few times the skin depth ( $l_s \approx 0.07\lambda_0$ ), as shown in Fig. 6(a).  $k_B T_e$  (approximately 22.5 MeV) at  $r_0 = 0.2\lambda_0$  is not the highest, but it corresponds to the optimal  $k_B T_{\gamma}$  (approximately 15.6 MeV), as seen in Figs. 3(a) and 3(c). This will result in the highest  $N_n$  at  $r_0 = 0.2\lambda_0$ . For given  $r_0$ , Fig. 6(b) indicates that there also exists an optimal  $d_0$ . This is because the blocking effect will occur if  $d_0 \leq 2\lambda_0$ ; conversely,  $E_{\gamma}$  at the wire surfaces is not great enough to pull out sufficient electrons when  $d_0$  is too large [39]. We see that the most neutrons are produced at  $d_0 = 1.9\lambda_0$  since a large number of electrons with  $k_B T_e = 22.5$  MeV are generated in the interaction process. Note that  $d_0$  for the highest  $k_B T_e$  is larger than  $1.9\lambda_0$ , which is different from that for the optimal  $N_e$ . This is because the electrons are easier to accelerate to higher energies when fewer electrons are trapped in the  $E_x^{\text{TM}}$  field of TM modes. This phenomenon is similar to the beam-loading effect in laser wakefield acceleration of electrons [1]. In addition to  $r_0$  and  $d_0$ ,  $L_0$  is also of great importance for electron acceleration and neutron generation. To obtain greater  $t_d$ , the wire should be of sufficient length since  $t_d$  is usually much greater than  $L_0/c$  for small  $d_0$  [23]. Figure 6(c) shows that  $L_0$  is at least  $10\lambda_0$  when  $r_0 = 0.2\lambda_0$  and  $d_0 = 1.9\lambda_0$ . With increasing  $L_0$ , we find that  $N_e$ ,  $k_B T_e$ , and  $N_n$  grow slowly because of the nearly depleted laser energy. Furthermore, we also notice



that  $N_e$  is slightly reduced, which is because many of the electrons with low energies counted in our simulation are actually from the Cu end plate. For greater  $L_0$ , almost all the laser energy is used to pull out and accelerate the wire electrons, resulting in less energy impacting on the end plate. Besides, we also simulate the case of different  $n_e$  values, and the results show that  $N_e$ ,  $k_B T_e$ , and  $N_n$  remain nearly unchanged, as shown in Fig. 6(d). This is because, for given  $a_0$ ,  $l_s$  (proportional to  $1/\sqrt{n_e}$ ) becomes larger as  $n_e$  decreases; conversely,  $l_s$  is smaller for higher  $n_e$ . The total number of electrons pulled out from the skin layer is almost comparable for different  $n_e$  values.

Actually, a preplasma can be formed between these Cu wires when the laser prepulse or amplified spontaneous emission interacts with the MST. To explore the effect of a preplasma on  $N_n$ , we perform simulations with uniform preplasmas of different densities filling the gaps between the wires [i.e., the MST-with-preplasma (MSTP) case]. Figures 7(a) and 7(b) show the spectra of electrons and neutrons at five preplasma densities of  $n_{e,p} = 0, 0.5n_c, 1.0n_c, 2.0n_c,$  and  $5.0n_c$ . We note that the influence of the preplasma on electron generation and neutron generation is negligible if  $n_{e,p} < 2n_c$ . However, for higher  $n_{e,p}$ , electron generation is obviously suppressed because more laser energy is consumed in the preplasma and thus cannot be fully used to pull out and accelerate dense electron bunches. This results in a decrease of  $N_n$  since photoneutron generation depends on  $N_e$  and  $k_B T_e$ . For comparison, we also simulate the case of a planar target with a preplasma (PTP), as shown in Figs. 7(c) and 7(d). The preplasma before the PT is of length  $10\lambda_0$ , which is the same as  $L_0$  in the MSTP case. One can see that  $N_e$  and  $N_n$  for the MSTP case are much greater than in the PTP case when  $n_{e,p} < 2n_c$ . However, they will be comparable with increasing  $n_{e,p}$  because the betatron resonant absorption begins to dominate the electron-heating process for the PTP case [50,51]. Usually,  $n_{e,p}$  is relatively low for an USUI laser pulse with high contrast [52]. The MST is therefore beneficial for hot-electron generation and neutron generation. For experiments, it is important to keep the wires intact, which requires that the laser contrast is at least  $10^{10}$ , as shown in recent experiments [21,24,29,53–55]. Fortunately, an USUI laser pulse of intensity greater than  $10^{20}$  W/cm<sup>2</sup> and contrast up to  $10^{12}$  is available [29]. Our proposed scheme should be realizable in the laboratory with existing technology.

#### IV. CONCLUSION

In summary, we propose a highly efficient scheme for producing a photoneuclear pulsed neutron source by irradiating a microstructure target with an ultraintense femtosecond laser pulses combined with a high- $Z$  converter. The interaction process is investigated by three-dimensional PIC and MC simulations. It is found that the transverse

electric field of the laser can pull out dense electron bunches from the wires. These electrons can be synergistically accelerated forward by the ponderomotive force of the laser and the longitudinal electric field of the excited TM modes between the adjacent wires. When they pass through the subsequent high- $Z$  converter, a large number of photons and neutrons are generated by bremsstrahlung radiation and photonuclear reaction, respectively. For optimized microstructure parameters, the neutron yield per joule of laser energy is as high as approximately  $2 \times 10^8$  J<sup>-1</sup> and the pulse duration is as short as approximately 45 ps. This yield is almost 1 order of magnitude higher than the record  $1.1 \times 10^7$  J<sup>-1</sup> for a laser-driven photoneuclear neutron source reported to date. A simple analytical model is established to predict the neutron yield, which is fairly consistent with the simulation result. Our scheme offers a relatively simple route to produce high-yield neutrons for applications such as fast-neutron resonance radiography, neutron therapy, and fusion-material research.

#### ACKNOWLEDGMENTS

This work was supported by the National Key R&D Program of China (Grant No. 2018YFA0404802), the National Natural Science Foundation of China (Grants No. 11705280, No. 11675264, No. 11475259, No. 11774430, and No. 12075157), the Natural Science Foundation of Hunan Province (Grant No. 2020JJ5031), the Science and Technology on plasma physics Laboratory (Grant No. 6142A04190111), and the Research Project of NUDT (Grants No. ZK18-03-09, No. ZK19-22, and No. ZK18-02-02). D.B.Z. also acknowledges the financial support from NUDT Young Innovator Awards (Grant No. 20190102) and Teaching Reform Program for Advanced Electrodynamics.

- 
- [1] E. Esarey, C. B. Schroeder, and W. P. Leemans, Physics of laser-driven plasma-based electron accelerators, *Rev. Mod. Phys.* **81**, 1229 (2009).
  - [2] H. Daido, M. Nishiuchi, and A. S. Pirozhkov, Review of laser-driven ion sources and their applications, *Rep. Prog. Phys.* **75**, 056401 (2012).
  - [3] M. Roth *et al.*, Bright Laser-Driven Neutron Source Based on the Relativistic Transparency of Solids, *Phys. Rev. Lett.* **110**, 044802 (2013).
  - [4] S. R. Mirfayzi *et al.*, Experimental demonstration of a compact epithermal neutron source based on a high power laser, *Appl. Phys. Lett.* **111**, 044101 (2017).
  - [5] X. R. Jiang, F. Q. Shao, D. B. Zou, M. Y. Yu, L. X. Hu, X. Y. Guo, T. W. Huang, H. Zhang, S. Z. Wu, G. B. Zhang, T. P. Yu, Y. Yin, H. B. Zhuo, and C. T. Zhou, Energetic deuterium-ion beams and neutron source driven by multiple-laser interaction with pitcher-catcher target, *Nucl. Fusion* **60**, 076019 (2020).



- [6] P. L. Shkolnikov, A. E. Kaplan, A. Pukhov, and J. Meyer-ter-Vehn, Positron and gamma-photon production and nuclear reactions in cascade processes initiated by a sub-terawatt femtosecond laser, *Appl. Phys. Lett.* **71**, 3471 (1997).
- [7] K. W. D. Ledingham *et al.*, Photonuclear Physics When a Multiterawatt Laser Pulse Interacts with Solid Targets, *Phys. Rev. Lett.* **84**, 899 (2000).
- [8] I. Pomerantz, E. McCary, A. R. Meadows, A. Arefiev, A. C. Bernstein, C. Chester, J. Cortez, M. E. Donovan, G. Dyer, E. W. Gaul, D. Hamilton, D. Kuk, A. C. Lestrade, C. Wang, T. Ditmire, and B. M. Hegelich, Ultrashort Pulsed Neutron Source, *Phys. Rev. Lett.* **113**, 184801 (2014).
- [9] X. J. Jiao, J. M. Shaw, T. Wang, X. M. Wang, H. Tsai, P. Poth, I. Pomerantz, L. A. Labun, T. Toncian, M. C. Downer, and B. M. Hegelich, A tabletop ultrashort pulse photoneutron source driven by electrons from laser wakefield acceleration, *Matter Radiat. Extremes* **2**, 296 (2017).
- [10] D. Vartsky, I. Mor, M. B. Goldberg, D. Bar, G. Feldman, V. Dangendorf, K. Tittelmeier, M. Weierganz, B. Bromberger, and A. Breskin, Novel detectors for fast-neutron resonance radiography, *Nucl. Instrum. Methods A* **623**, 603 (2010).
- [11] A. Wittig, J. Michel, R. L. Moss, F. Stecher-Rasmussen, H. F. Arlinghaus, P. Bendel, P. L. Mauri, S. Altieri, R. Hilger, P. A. Salvadori, L. Menichetti, R. Zamenhof, and W. A. G. Sauerwein, Boron analysis and boron imaging in biological materials for Boron Neutron Capture Therapy (BNCT), *Crit. Rev. Oncol. Hematol.* **68**, 66 (2008).
- [12] G. Zaccai, How soft is a protein? A protein dynamics force constant measured by neutron scattering, *Science* **288**, 1604 (2000).
- [13] Y. Arikawa *et al.*, High-intensity neutron generation via laser-driven photonuclear reaction, *Plasma Fusion Res.* **10**, 2404003 (2015).
- [14] W. Qi, X. H. Zhang, B. Zhang, S. K. He, F. Zhang, B. Cui, M. H. Yu, Z. H. Dai, X. Y. Peng, and Y. Q. Gu, Enhanced photoneutron production by intense picoseconds laser interacting with gas-solid hybrid targets, *Phys. Plasmas* **26**, 043103 (2019).
- [15] F. H. Ruddy, R. W. Flammang, and J. G. Seidels, Low-background detection of fission neutrons produced by pulsed neutroninterrogation, *Nucl. Instrum. Methods A* **518**, 603 (2009).
- [16] A. Lepretre, H. Beil, R. Bergere, P. Carlos, J. Fagot, A. De Miniac, and A. Veyssiere, Measurements of the total photonuclear cross sections from 30 MeV to 140 MeV for Sn, Ce, Ta, Pb and U nuclei, *Nucl. Phys. A* **367**, 237 (1981).
- [17] B. L. Berman and S. C. Fultz, Measurements of the giant dipole resonance with monoenergetic photons, *Rev. Mod. Phys.* **47**, 713 (1975).
- [18] C. G. R. Geddes, Cs. Toth, J. van Tilborg, E. Esarey, C. B. Schroeder, D. Bruhwiler, C. Nieter, J. Cary, and W. P. Lee-mans, High-quality electron beams from a laser wakefield accelerator using plasma-channel guiding, *Nature* **431**, 538 (2004).
- [19] S. C. Wilks and W. L. Kruer, Absorption of ultrashort, ultra-intense laser light by solids and overdense plasmas, *IEEE J. Quantum Electron.* **33**, 1954 (1997).
- [20] A. Macchi, M. Borghesi, and M. Passoni, Ion acceleration by superintense laser-plasma interaction, *Rev. Mod. Phys.* **85**, 751 (2013).
- [21] S. Jiang, L. L. Ji, H. Audesirk, K. M. George, J. Snyder, A. Krygier, P. Poole, C. Willis, R. Daskalova, E. Chowdhury, N. S. Lewis, D. W. Schumacher, A. Pukhov, R. R. Freeman, and K. U. Akli, Microengineering Laser Plasma Interactions at Relativistic Intensities, *Phys. Rev. Lett.* **116**, 085002 (2016).
- [22] Z. Gong, A. P. L. Robinson, X. Q. Yan, and A. V. Arefiev, Highly collimated electron acceleration by longitudinal laser fields in a hollow-core target, *Plasma Phys. Controlled Fusion* **61**, 035012 (2019).
- [23] D. B. Zou, D. Y. Yu, M. Y. Yu, T. W. Huang, A. Pukhov, H. B. Zhuo, C. T. Zhou, and S. C. Ruan, Efficient generation of  $\sim 100$  MeV ions from ultrashort  $\sim 10^{21}$  W cm $^{-2}$  laser pulse interaction with a waveguide target, *Nucl. Fusion* **59**, 066034 (2019).
- [24] G. Cristoforetti, F. Baffigi, F. Brandi, G. D'Arrigo, A. Fazzi, L. Fulgentini, D. Giove, P. Koester, L. Labate, G. Maero, D. Palla, M. Romé, R. Russo, D. Terzani, P. Tomassini, and L. A. Gizzi, Laser-driven proton acceleration via excitation of surface plasmon polaritons into TiO $_2$  nanotube array targets, *Plasma Phys. Controlled Fusion* **62**, 114001 (2020).
- [25] Y. C. Wang, Y. Yin, W. Q. Wang, D. B. Zou, W. X. Miao, T. P. Yu, and F. Q. Shao, Copious positron production by femto-second laser via absorption enhancement in a microstructured surface target, *Sci. Rep.* **10**, 5861 (2020).
- [26] L. Q. Yi, A. Pukhov, P. Luu-Thanh, and B. F. Shen, Bright X-Ray Source from a Laser-Driven Microplasma Waveguide, *Phys. Rev. Lett.* **116**, 115001 (2016).
- [27] B. Feng, C. Y. Qin, X. S. Geng, Q. Yu, W. Q. Wang, Y. T. Wu, X. Yan, L. L. Ji, and B. F. Shen, The emission of  $\gamma$ -Ray beams with orbital angular momentum in laser-driven micro-channel plasma target, *Sci. Rep.* **9**, 18780 (2019).
- [28] M. Bailly-Grandvaux, D. Kawahito, C. McGuffey, J. Strehlow, B. Edghill, M. S. Wei, N. Alexander, A. Haid, C. Brabetz, V. Bagnoud, R. Hollinger, M. G. Capeluto, J. J. Rocca, and F. N. Beg, Ion acceleration from microstructured targets irradiated by high-intensity picosecond laser pulses, *Phys. Rev. E* **102**, 021201(R) (2020).
- [29] A. Curtis, C. Calvi, J. Tinsley, R. Hollinger, V. Kaymak, A. Pukhov, S. J. Wang, A. Rockwood, Y. Wang, V. N. Shlyaptsev, and J. J. Rocca, Micro-scale fusion in dense relativistic nanowire array plasmas, *Nat. Commun.* **9**, 1077 (2018).
- [30] C. P. Ridgers, C. S. Brady, R. Ducloux, J. G. Kirk, K. Bennett, T. D. Arber, A. P. L. Robinson, and A. R. Bell, Dense Electron-Positron Plasmas and Ultraintense  $\gamma$  Rays from Laser-Irradiated Solids, *Phys. Rev. Lett.* **108**, 165006 (2012).
- [31] A. Pukhov, Strong field interaction of laser radiation, *Rep. Prog. Phys.* **66**, 47 (2003).
- [32] G. Battistoni, F. Cerutti, A. Fassò, A. Ferrari, S. Muraro, J. Ranft, S. Roesler, and P. R. Sala, The FLUKA code: Description and benchmarking, AIP Conf. Proc. 896, 31 (2007).

- [33] T. Kluge, S. A. Gaillard, K. A. Flippo, T. Burris-Mog, W. Enghardt, B. Gall, M. Geissel, A. Helm, S. D. Kraft, T. Lockard, J. Metzkes, D. T. Offermann, M. Schollmeier, U. Schramm, K. Zeil, M. Bussmann, and T. E. Cowan, High proton energies from cone targets: Electron acceleration mechanisms, *New J. Phys.* **14**, 023038 (2012).
- [34] L. L. Ji, J. Snyder, A. Pukhov, R. R. Freeman, and K. U. Akli, Towards manipulating relativistic laser pulses with micro-tube plasma lenses, *Sci. Rep.* **6**, 23256 (2016).
- [35] D. B. Zou, A. Pukhov, L. Q. Yi, H. B. Zhou, T. P. Yu, Y. Yin, and F. Q. Shao, Laser-driven Ion acceleration from plasma micro-channel targets, *Sci. Rep.* **7**, 42666 (2017).
- [36] J. Q. Yu, R. H. Hu, Z. Gong, A. Ting, Z. Najmudin, D. Wu, H. Y. Lu, W. J. Ma, and X. Q. Yan, The generation of collimated  $\gamma$ -ray pulse from the interaction between 10 PW laser and a narrow tube target, *Appl. Phys. Lett.* **112**, 204103 (2018).
- [37] L. X. Hu, T. P. Yu, Z. M. Sheng, J. Vieira, D. B. Zou, Y. Yin, P. McKenna, and F. Q. Shao, Attosecond electron bunches from a nanofiber driven by laguerre-gaussian laser pulses, *Sci. Rep.* **8**, 7282 (2018).
- [38] N. Naumova, I. Sokolov, J. Nees, A. Maksimchuk, V. Yanovsky, and G. Mourou, Attosecond Electron Bunches, *Phys. Rev. Lett.* **93**, 195003 (2004).
- [39] D. Y. Yu, D. B. Zou, M. Y. Yu, T. P. Yu, Y. Yin, F. Q. Shao, H. B. Zhuo, C. T. Zhou, and S. C. Ruan, Generation of relativistic high-order-mode laser pulse using plasma waveguide, *New J. Phys.* **21**, 083003 (2019).
- [40] M. C. Levy, S. C. Wilks, M. Tabak, S. B. Libby, and M. G. Baring, Petawatt laser absorption bounded, *Nat. Commun.* **5**, 4149 (2014).
- [41] <https://www.nndc.bnl.gov/>.
- [42] S. C. Wilks, A. B. Langdon, T. E. Cowan, M. Roth, M. Singh, S. Hatchett, M. H. Key, D. Pennington, A. MacKinnon, and R. A. Snavely, Energetic proton generation in ultra-intense laser-solid interactions, *Phys. Plasmas* **8**, 542 (2001).
- [43] T. Kluge, T. Cowan, A. Debus, U. Schramm, K. Zeil, and M. Bussmann, Electron Temperature Scaling in Laser Interaction with Solids, *Phys. Rev. Lett.* **107**, 205003 (2011).
- [44] F. N. Beg, A. R. Bell, A. E. Dangor, C. N. Danson, A. P. Fewes, M. E. Glinsky, B. A. Hammel, P. Lee, P. A. Norreys, and M. Tatarakis, A study of picosecond laser-solid interactions up to  $10^{19}$  W/cm<sup>2</sup>, *Phys. Plasmas* **4**, 447 (1997).
- [45] M. G. Haines, M. S. Wei, F. N. Beg, and R. B. Stephens, Hot-Electron Temperature and Laser-Light Absorption in Fast Ignition, *Phys. Rev. Lett.* **102**, 045008 (2009).
- [46] D. J. S. Findlay, Analytic representation of bremsstrahlung spectra from thick radiators as a function of photon energy and angle, *Nucl. Phys. A* **276**, 598 (1989).
- [47] S. M. Seltzer and M. J. Berger, Bremsstrahlung energy spectra from electrons with kinetic energy 1 keV-10 GeV incident on screened nuclei and orbital electrons of neutral atoms with  $Z = 1 - 100$ , *At. Data Nucl. Data Tables A* **35**, 345 (1986).
- [48] M. J. Berger and S. M. Seltzer, Bremsstrahlung and photoneutrons from thick tungsten and tantalum targets, *Phys. Rev. C* **2**, 621 (1970).
- [49] L. Pages, E. Bertel, H. Joffre, and L. Sklaventis, Energy loss, range, and bremsstrahlung yield for 10-keV to 100-MeV electrons in various elements and chemical compounds, *At. Data Nucl. Data Tables A* **4**, 1 (1972).
- [50] A. Pukhov, Z. M. Sheng, and J. Meyer-ter-Vehn, Particle acceleration in relativistic laser channels, *Phys. Plasmas* **6**, 2847 (1999).
- [51] D. B. Zou, H. B. Zhuo, X. H. Yang, F. Q. Shao, Y. Y. Ma, T. P. Yu, H. C. Wu, Y. Yin, Z. Y. Ge, and X. H. Li, Enhanced target normal sheath acceleration based on the laser relativistic selffocusing, *Phys. Plasmas* **21**, 063103 (2014).
- [52] X. L. Ge, X. X. Lin, X. H. Yuan, D. C. Carroll, R. J. Gray, T. P. Yu, O. Tresca, M. Chen, F. Liu, H. B. Zhuo, B. Zielbauer, L. Zhao, D. Neely, Z. M. Sheng, Y. T. Li, and P. McKenna, Directed fast electron beams in ultraintense picosecond laser irradiated solid targets, *Appl. Phys. Lett.* **107**, 091111 (2015).
- [53] C. Bargsten, R. Hollinger, M. G. Capeluto, V. Kaymak, A. Pukhov, S. J. Wang, A. Rockwood, Y. Wang, D. Keiss, R. Tommasini, R. London, J. Park, M. Busquet, M. Klapisch, V. N. Shlyaptsev, and J. J. Rocca, Energy penetration into arrays of aligned nanowires irradiated with relativistic intensities: Scaling to terabar pressures, *Sci. Adv.* **3**, e1601558 (2017).
- [54] J. Snyder, L. L. Ji, K. M. George, C. Willis, G. E. Cochran, R. L. Daskalova, A. Handler, T. Rubin, P. L. Poole, D. Nasir, A. Zingale, E. Chowdhury, B. F. Shen, and D. W. Schumacher, Relativistic laser driven electron accelerator using micro-channel plasma targets, *Phys. Plasmas* **26**, 033110 (2019).
- [55] L. A. Gizzi, G. Cristoforetti, F. Baffigi, F. Brandi, G. D'Arrigo, A. Fazzi, L. Fulgentini, D. Giove, P. Koester, L. Labate, G. Maero, D. Palla, M. Romé, M. Russo, D. Terzani, and P. Tomassini, Intense proton acceleration in ultrarelativistic interaction with nanochannels, *Phys. Rev. Res.* **2**, 033451 (2020).